Materials Science & Engineering A 822 (2021) 141665

Contents lists available at ScienceDirect

Materials Science & Engineering A

journal homepage: www.elsevier.com/locate/msea

The role of thermomechanical processing routes on the grain boundary network of martensite in Ti–6Al–4V

Ehsan Farabi [a], Vahid Tari [b], Peter D. Hodgson [a], Gregory S. Rohrer [b], Anthony D. Rollett [b], Hossein Beladi [a,*]

[a] Institute for Frontier Materials, Deakin University, Geelong, Victoria, 3216, Australia
[b] Department of Materials Science and Engineering, Carnegie Mellon University, Pittsburgh, PA, 15213-3890, USA

ARTICLE INFO

Keywords:
Titanium
Therrmomechanical processing
Texture
Variant selection
Intervariant boundary plane character distribution
Visco-plastic self-consistent modelling

ABSTRACT

The influence of thermomechanical processing (TMP) of a Ti–6Al–4V alloy on the transformation texture and intervariant boundary network were investigated by conventional EBSD mapping along with the five-parameter boundary analysis approach. The texture characteristics of Ti–6Al–4V subjected to deformation in the β regime followed by the $\beta \rightarrow \alpha$ martensitic transformation were examined using visco-plastic self-consistent simulation and forward calculation of the transformation texture. Comparison of the simulated and experimental texture characterisitcs revealed that the transformed α' texture was dominated by the variant selection associated with substructure development in the β parent phase and the occurrence of specific self-accommodating α' variants in the microstructure, promoting the quadrilateral and/or V shape variant arrangement. This resulted in a progressive increase in the 63.26°/[$\bar{1}0553$] intervariant boundaries with the strain increment, at the expense of 60°/[1 1 $\bar{2}$0]. Moreover, the grain boundary network for all conditions was dominated by the triple junctions (grain boundary network) terminating on 63.26°/[$\bar{1}0553$] and 60°/[1 1 $\bar{2}$0] intervariants. It is shown that the elastic interactions among the variants during the martensitic transformation is the dominant parameter affecting the grain boundary network, despite the presence of dislocation based variant selection.

1. Introduction

Titanium alloys, Ti–6Al–4V in particular, are important materials for the aerospace, defence, biomedical, and maritime industry sectors [1,2]. They present a unique combination of properties, namely high strength to weight ratio, corrosion resistance and biocompatibility, but high manufacturing expenses have limited their application. Thermomechanical processing (TMP) is known to be one of the most generally accepted and cost-effective approaches to control the microstructure and properties of Ti6Al–4V [3]. TMP of Ti alloys is largely conducted in the single phase β (bcc) region, where the ingot structure is broken down, followed by a secondary grain refinement process in the two phase α (hcp) + β (bcc) region [4,5]. Therefore, the morphological features of the α and β phases and texture characteristics developed by primary recrystallization, grain growth and the α → β phase transformation during TMP have a strong effect on the physical and mechanical performance of a semi-finished or finished Ti–6Al–4V product [6–9].

The β → α phase transformation that occurs during Ti processing strictly follows the Burgers crystallographic orientation relationship (OR), producing 12 distinct α variants from a given parent β grain [10]. The fraction of available variants and their corresponding intersections (known as variant selection) can significantly influence the overall texture and α/α grain boundary characteristics of the Ti alloy [11–16]. The variant selection is strongly influenced by the crystallographic constraints of the transformation mechanism [16,17], the related transformation energy [15,18,19] and the externally applied deformation that changes the state of the parent β phase [14]. The role of the phase transformation path and composition on the variant selection, texture evolution and grain boundary network has been extensively studied in Ti alloys [20–23]. The elastic energy of the martensitic transformation is largely accommodated through characteristic

* Corresponding author.
E-mail address: hossein.beladi@deakin.edu.au (H. Beladi).

https://doi.org/10.1016/j.msea.2021.141665
Received 24 April 2021; Received in revised form 21 June 2021; Accepted 26 June 2021
Available online 29 June 2021
0921-5093/© 2021 Elsevier B.V. All rights reserved.

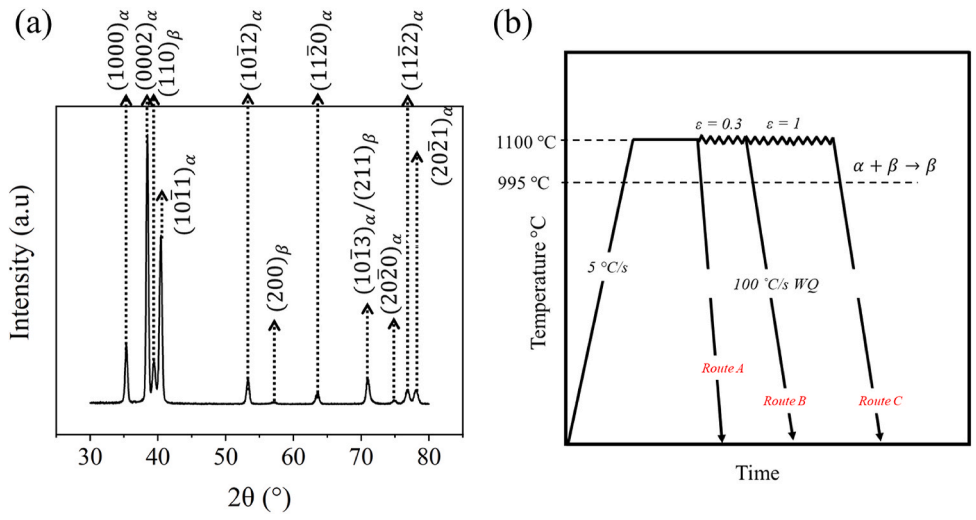

Fig. 1. (a) The XRD pattern obtained from as-rolled Ti–6Al–4V alloy revealing both α and β phase peaks, and (b) schematic illustration of the heat treatment procedure.

Table 1
The EBSD parameters used for microstructures produced through different TMP routes.

TMP condition	EBSD condition		
	Step size (μm)	EBSD area	Line segments
Strain-free	0.01	49 × 6 μm × 6 μm	~140,000
Strained to 0.3	0.01	27 × 6 μm × 6 μm	~120,000
Strained to 1	0.01	26 × 6 μm × 6 μm	~120,000

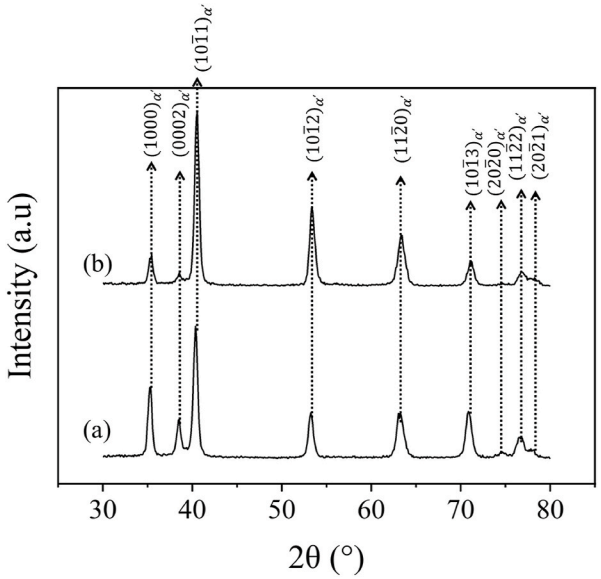

Fig. 2. XRD patterns corresponding to the Ti–6Al–4V alloy at (a) strain of 0.3 and (b) strain of 1 conditions.

groupings of α′ variants, promoting a specific α′/α′ intervariant boundary network [16,20,22]. This local variant selection mechanism is strongly influenced by the crystallographic parameters of the parent β and daughter α′ phases in martensitic Ti alloys, as it can alter the elastic strain energy during the shear transformation. Therefore, a small change in chemical composition influences the transformation strain energy leading to various α′ clusters and the intervariant boundary network [21,22]. Consequently, 3 variant cluster formation in martensitic pure Ti increases the population and connectivity of twin related 60°/[1 1 $\bar{2}$ 0] intervariants with a symmetric tilt (1 0 $\bar{1}$ 1) character [21,23]. Four variant clusters promote the 63.26°/[$\bar{1}$0 5 5 $\bar{3}$] intervariants with ($\bar{3}$210) twist character during the martensitic transformation of Ti–6Al–4V [22,24,25]. Changing the transformation mechanism as the cooling rate decreases from shear to diffusion assisted (i.e., Widmanstätten) and diffusional transformation reduces this local variant selection mechanism to such an extent that no specific variant arrangement dominates [20]. This can result in a significant decrease in the population and connectivity of low energy 60°/[1 1 $\bar{2}$ 0] intervariants in pure Ti, leading to a relatively random distribution of intervariant boundaries [20].

Aside from the transformation characteristics, the state of the prior β phase (i.e., grain size, texture and deformation structure) has a strong influence on the variant selection mechanism during the subsequent β→α transformation [14,15,26–28]. In other words, the magnitude of the variant selection during the transformation has been shown to be significantly affected by the processing variables [14,29–31]. Different strain levels during the hot working process can change the parent phase texture and substructure characteristics, leading to different levels of variant selection [30,32]. Gey et al. [30] showed that the selected variants are mostly associated with the most active β phase slip systems at higher rolling reductions. In parallel, Semiatin et al. [32] showed that straining the β phase prior to transformation can lead to noticeable variant selection. It was shown that lower rolling reductions do not favor particular variants and the resulting texture approaches the theoretical distribution of *α* variants expected from the Burgers OR [32]. In addition, the strain field associated with dislocation/s [29,33,34] and their characteristics (i.e., screw, edge and mixed) [14] can promote preferential variant nucleation, thus influencing the variant selection. Such variation in the variant selection through changes in the state of the β phase is expected to result in different intervariant boundary characteristics.

In the current study, the influence of the thermomechanical processing of a Ti–6Al–4V alloy on the intervariant boundary network characteristics is investigated. To this end, the material was subjected to different TMP sequences above the β transus, followed by transformation to martensite (at high cooling rate). Considering the β to α′ transformation, the nucleated variant can be correlated to the parent β orientations being developed by the most active slip systems in the bcc structured phases. Therefore, texture evolution during TMP is simulated by a visco-plastic self-consistent (VPSC) model for active bcc slip systems [35,36]. Moreover, the simulated α′ textures were analysed based on experimental texture characteristics to define the influence of the TMP route on the variant selection and grain boundary network in Ti alloys. Finally, the grain boundary network characteristics were also examined using the five-parameter grain boundary analysis approach

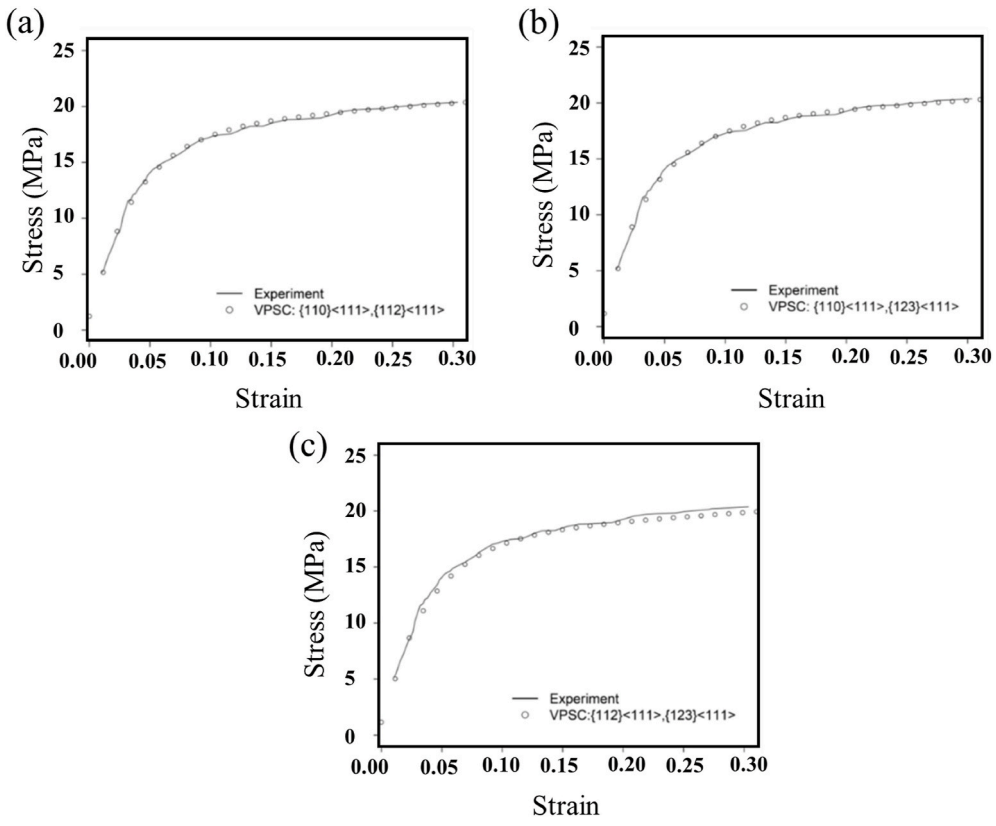

Fig. 3. The calibrated (circles) stress–strain curves using the combination of (a) {110}<111> and {112}<111>, (b) {110}<111> and {123}<111>, (c) {112}<111> and {123}<111> slip systems and their corresponding experimental stress-strain curves.

Table 2
Voce hardening parameters and velocity gradient for plane strain (rolling).

	τ_0	τ_1	θ_0	θ_1	Velocity gradient
{110}<111>	1	14.7	120	1.9	$\begin{bmatrix}1&0&0\\0&0&0\\0&0&-1\end{bmatrix}$
{112}<111>	1.5	6.9	80	1.1	
{123}<111>	1.8	12	85	1.4	

along with triple junction classification as a function of intervariant boundary type. The current findings enable us to uncover the potential of TMP for grain boundary network engineering in Ti alloys.

2. Experimental procedure

2.1. Material

The as-received material comprised several 5.75 mm thick hot rolled plates, having a composition close to the nominal Ti–6Al–4V alloy. The as-hot rolled material contained both α and β phases (Fig. 1a), as confirmed by XRD (Fig. 1b). Plane strain compression samples (with dimensions 60 mm × 20 mm × 5 mm were cut from the as-received plate where the 60 mm length was parallel to the rolling direction. The samples were coated with glass-based coating (Acheson's Deltaglaze FB-412) to minimise oxidation at high temperatures. They were reheated to the fully β-phase region at 1100 °C and held isothermally for 180 s before being subjected to plane strain compression up to levels of 0, 0.3 and 1 at a strain rate of 0.1/s. Then, they were immediately water-quenched to obtain a fully martensitic α′ structure (see Routes A through C in Fig. 1b). Route A corresponds to the martensitic Ti–6Al–4V

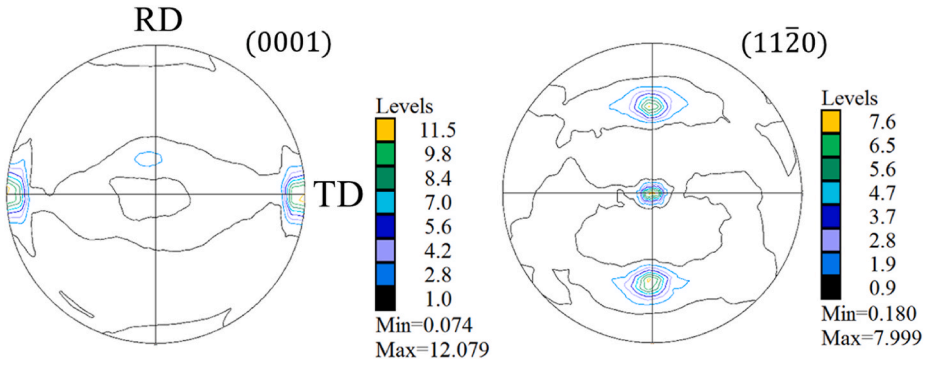

Fig. 4. The basal and prismatic pole figures of the as received Ti–6Al–4V plate.

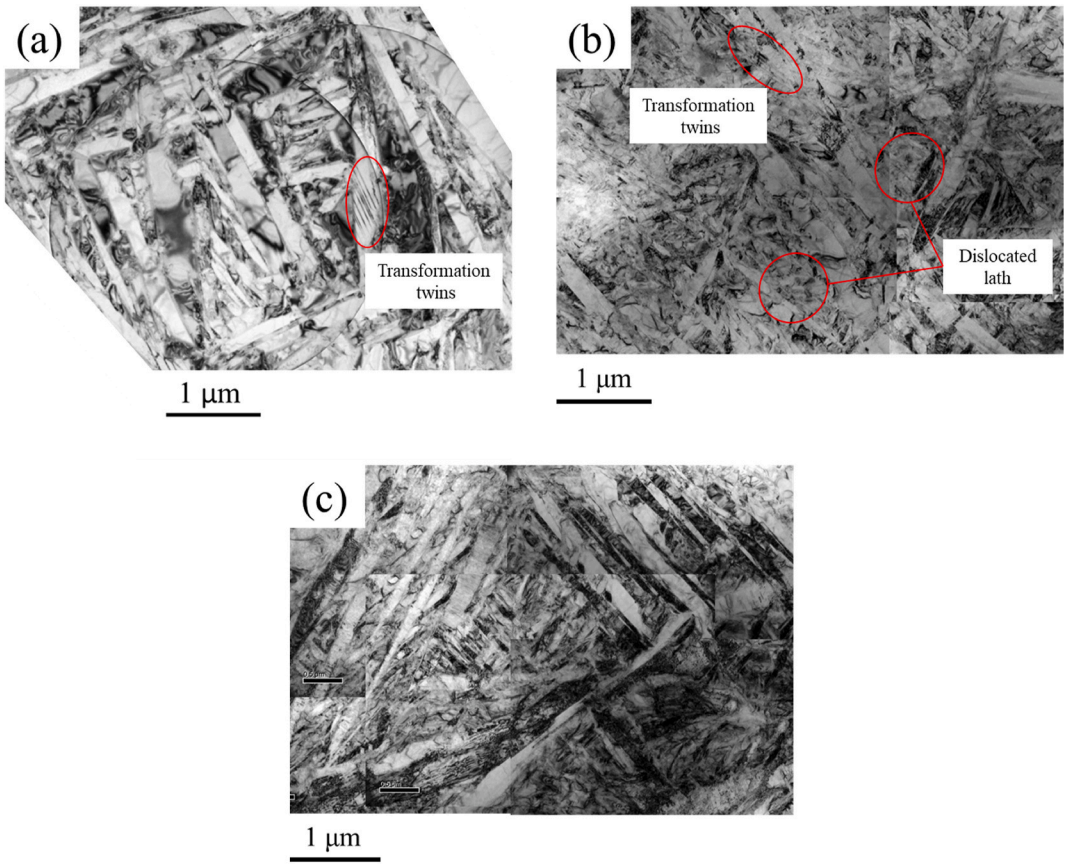

Fig. 5. The bright field TEM observations of the martensitic microstructure obtained at different thermomechanical processing routes of (a) strain-free, (b) strain of 0.3 and (c) strain of 1.

sample formed in a strain-free condition, while the material experiences strains of 0.3 and 1 for routes B and C, respectively. All the thermomechanical schedules were conducted using a computer controlled Servotest TMTS (servo-hydraulic deformation simulator) machine. It should be mentioned that the strain of 0.6 was also conducted in the current study. However, the obtained results at 0.6 strain were close to the strain 1. Therefore, the data obtained for this TMP route was not investigated further.

2.2. Microstructural characterization

The microstructures of the thermomechanically processed samples were examined using electron backscatter diffraction (EBSD). However, for a better quantitative characterization and a higher spatial resolution of the developed microstructure (i.e., the very thin martensitic α′-laths) in hot-deformed samples, a step size as small as 10 nm was needed. To this end, the transmission Kikuchi diffraction (TKD) technique was used to examine the microstructure of the samples. Two perpendicular cross-sections, namely the rolling and normal direction (RD-ND section) and the rolling and transverse direction (RD-TD section) were taken for microstructure examination.

For transmission electron microscopy (TEM), a similar sample preparation method was employed. The samples cut from both cross sections were initially ground to a thickness of 120 μm and then punched to make foils with a 3 mm diameter. The foils were further mechanically ground to a thickness of ~50 μm followed by twin-jet electropolishing using a solution containing 6% perchloric acid and 35% butoxy-methanol and 64% methanol at a temperature of about −40 °C and a voltage of 35 V. The EBSD measurements were conducted in a FEG Quanta 3-D FEI SEM instrument using a 30 kV and 8 nA beam and an Oxford Instruments TKD sample holder. TSL software was used to acquire the EBSD data using a hexagonal grid. For each thermomechanical condition multiple, EBSD scans, with area of 6 μm × 6 μm, were performed with the step size of 10 nm (Table 1). The average confidence index of the obtained EBSD scanes were between 0.3 and 0.4. TSL OIM Analysis V6.1 software was used to perform to post-process the EBSD data. A comprehensive cleaning procedure for the acquired data was employed and then the boundary line traces/segments were extracted to measure the intervariant boundary plane orientations through a stereological approach, as described in Ref. [37]. As mentioned, the TKD analysis was conducted on two perpendicular sections (RD-ND and RD-TD) of the samples to reduce the texture bias in the distribution of intervariant boundary planes. More than 100,000 boundary segments were obtained for each thermomechanical condition, enabling a reliable calculation of the boundary plane orientation. The measured EBSD area and the number of boundary segments are summarised in Table 1 for each thermomechanical route.

2.2.1. Texture measurements

2.2.1.1. XRD analysis. A PANalytical X-ray diffractometer equipped with Cu-K_α radiation was used to measure the texture of the thermomechanically processed samples. The voltage and the current values were set at 40 kV and 30 nA, respectively. The constituent phases were analysed using the point scan settings and the typical peaks corresponding to the samples processed through different conditions, as depicted in Figs. 1a and 2.

The texture measurements were conducted on the rolling direction (RD)-transverse direction (TD) plane where TD was pointed towards the X-ray source. Moreover, to compensate for the large β grain size obtained during the heat treatment and consequently increase the statistical liability of the texture measurements, a large sample size (i.e., 30

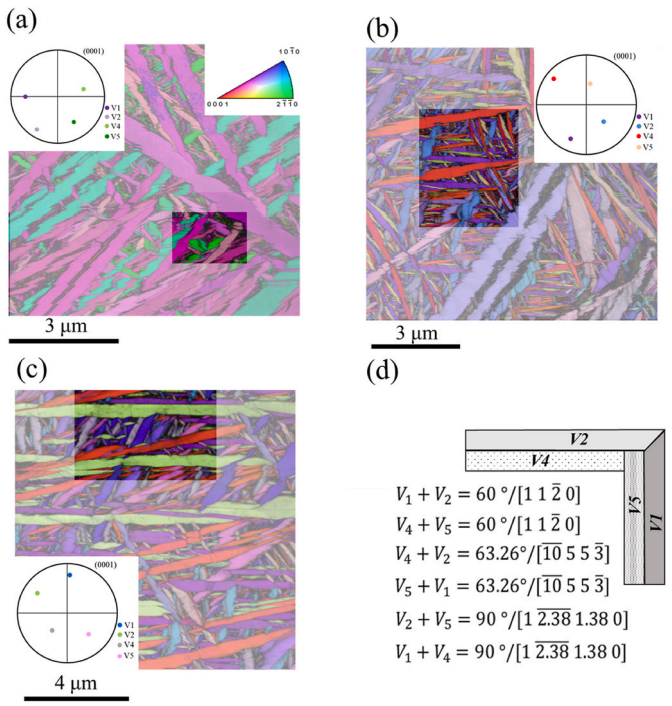

Fig. 6. The TKD imaging of the martensitic microstructure obtained through elaborating (a) no straining, (b) straining to 0.3, (c) straining to 1 and the schematic illustration of the observed local variant combinations, (d) schematic illustration of the martensitic lath clustering [21]. The colours are the orientations referred to the normal direction. (For interpretation of the references to colour in this figure legend, the reader is referred to the Web version of this article.)

mm × 30 mm) was prepared for the analysis. Six pole figures, namely $(1\,0\,\bar{1}\,0)$, $(0\,0\,0\,2)$, $(1\,0\,\bar{1}\,1)$, $(1\,0\,\bar{1}\,2)$, $(1\,0\,\bar{1}\,3)$ and $(1\,1\,\bar{2}\,0)$, were acquired satisfying the minimum representation of texture in hcp materials. A standard step size of 5° in tilt, 0-80°, and in azimuth 0-360° with 6s count time at each location as well as stage oscillation, with 5 mm linear movement, was employed for each pole figure. The LaboTex® software was used for post-processing of the XRD data files and the ODFs were calculated by the Arbitrarily Defined Cells (ADC) algorithm while applying orthorhombic sample symmetry.

2.2.1.2. Visco-plastic self-consistent (VPSC) modelling of texture evolution of β titanium. The evolution of the β phase texture during thermomechanical processing of the Ti–6Al–4V alloy at 1100 °C for strain levels of 0.3 and 1 was simulated using the visco-plastic self-consistent (VPSC) approach [36]. In this study, different combinations of 12 slip systems in $\{110\}_\beta\langle 111\rangle_\beta$, 12 slip systems in $\{211\}_\beta\langle 111\rangle_\beta$ and 24 slip systems in $\{123\}_\beta <111>_\beta$ were considered. The critical resolved shear stress (CRSS) is described by the extended Voce hardening law [38]:

$$\widehat{\tau}(\Gamma) = \tau_0 + (\tau_1 + \theta_1\Gamma)\left\{1 - \exp\left(-\frac{\Gamma|\theta_0|}{\tau_1}\right)\right\} \quad (1)$$

where Γ, τ_0, τ_1 θ_0, θ_1 are the total accumulated shear in the grain, the initial CRSS, the back-extrapolated CRSS, the initial hardening rate and the asymptotic hardening rate, respectively.

The initial texture was assumed based on the high temperature texture reported in earlier studies by our research group on the same material [23]. To take account of the interaction of each grain with the surrounding material on the texture prediction, tangent model based on another study was elaborated [39]. In reference [39] the tangent model provides the closest agreement in terms of texture components to the experimental results (i.e., the best overall texture prediction). Takajo et al. showed that at least two slip systems are required in VPSC simulation to correctly predict texture evolution in bcc materials [39].

The Voce hardening parameters were chosen for each slip system based on optimizing the fit between the experimental stress-strain curve and the computed behavior in plane strain for different combinations of slip modes (Fig. 3). Table 2 summarizes the four hardening parameters for each slip system, adjusted to fit the measured stress-strain curve.

2.2.1.3. Forward calculation of transformation texture. The transformation from parent β to daughter α phases ($\Delta g_{\beta\to\alpha}$) in titanium alloys occurs according to the Burgers OR [22,40]. Equation (2) describes the mathematical calculation of the theoretical α texture from the β phase texture after the phase transformation.

$$g_{di} = TO_i g_p \quad (2)$$

where g_p is the orientation of the parent phase and g_{di} represents the daughter phase orientation. T is the transformation matrix, representing the Burgers orientation relationship between the β and α phases. O_i represents the parent cubic phase symmetry operators, of which there 24 (proper operators). Interestingly, owing to the crystallographic orientation relationship (i.e., Burgers OR), the O_i and O_{i+1} symmetry operators produce the same crystallographic variants; consequently each β orientation transforms to 12 distinct α orientations or variants in the absence of variant selection.

3. Results

The hot rolled material largely revealed strong α-phase peaks along with weaker β phase peaks, as confirmed by the XRD measurement (Fig. 1a). The texture of the as-rolled Ti–6Al–4V alloy was similar to the typical textures expected from hot rolling of the alloy within the two phase α+β region (~900–960 °C), and is known as the transverse texture (T-texture) [9,41,42]. This was identified by a strong component perpendicular to the rolling direction (RD) and parallel to the transverse direction (TD) in the $(0001)_{\alpha'}$ pole figure (the intensity is ~12 times random, Fig. 4).

3.1. Microstructure and texture evolution

3.1.1. Microstructure

The microstructures that resulted from heat treatment route A (i.e., strain-free condition) and the thermomechanical routes of B (i.e., strain of 0.3) and C (i.e., strain of 1) showed a fully martensitic structure with fine laths having almost similar average sizes of 0.1 μm, 0.075 μm and 0.077 μm, respectively (Fig. 5). It should be mentioned that the thickness of the samples were measured using the stereographic correction for lath spacings obtained from the Channel5 software [43,44]. The martensitic laths formed through the different thermomechanical routes displayed a dense dislocation substructure along with twinned regions. The dislocation structure increase with an increase in straining at high temperature (Fig. 5). The martensite morphology for all routes was similar, having a V-like and/or quadrilateral groupings of martensitic α variants as the characteristic feature of the martensite in the Ti–6Al–4V alloy (compare highlighted region in Fig. 6a–c and the already reported data in Ref. [22]). The intersection of these variant arrangements largely promoted the $63.26°/[\bar{10}\,5\,5\,\bar{3}]$, $60°/[1\,1\,\bar{2}\,0]$ and $90°/[1\,\bar{2.38}\,1.38\,0]$ intervariant boundaries (Fig. 6d). The horizontal lines within the TKD maps are associated with small vibretions within the instrument environment and needs to be considered as artifacts of the measurement. Due to very limited population of these artifacts it can be considered that they have a limited role on the grain boundary measurement.

3.1.2. Texture

The $(0\,0\,0\,1)_{\alpha'}$ and $(1\,0\,\bar{1}\,0)_{\alpha'}$ pole figures for martensite produced through different TMP routes (Fig. 7) showed two main texture

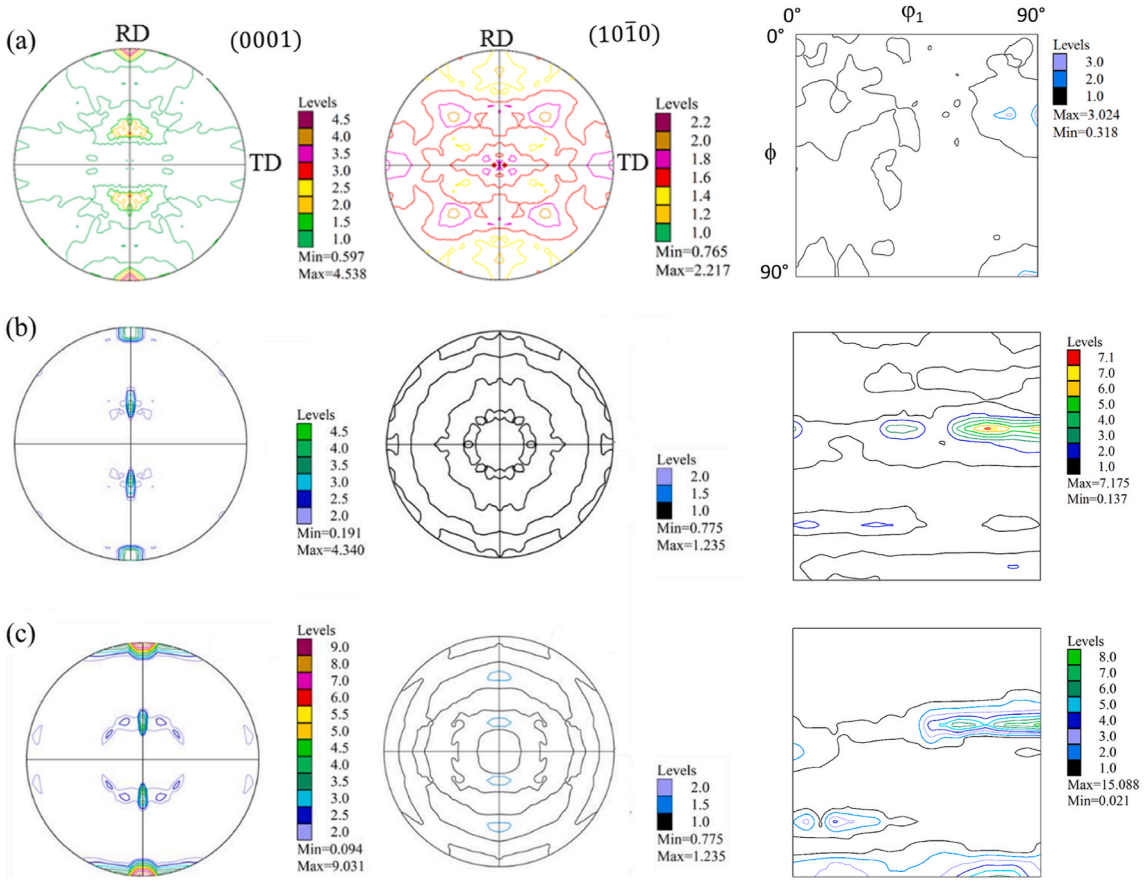

Fig. 7. The (0001) pole figures and $\phi 2 = 0°$ ODF section for the Ti–6Al–4V alloy samples subjected to different strains a) strain free, (b) 0.3, and c) 1.

Table 3
The relative intensity between the {90°, 30°, 0°}α' and {90°, 90°, 0°}α' components for experimental and simulated pole figures.

Active slip system	Strain free		Strain 0.3	Strain 1
	Exper.	Sim.		
Experimental	0.67	0.70	0.28	0.43
{110}<111> + {112}<111>	–		0.66	0.55
{110}<111> + {123}<111>	–	–	0.68	0.57
{112}<111> + {123}<111>	–	–	0.69	0.44
{110}<111> + {112}<111> + {123}<111>	–	–	0.69	0.58

components, namely the {90°, 90°, 0}$_{\alpha'}$ and {90°, 30°, 0}$_{\alpha'}$ for all TMP conditions. These components and their corresponding intensities are summarised in Table 3. It should be noted that the poles were plotted within ±5° of accuracy.

For the strain-free condition, the dominant orientation was the {90°, 90°, 0} $_{\alpha'}$ component having an intensity of ~4.5 times random in the $(0001)_{\alpha'}$ pole figure and ~2.2 in the corresponding $\phi_2 = 0°$ section (Fig. 7a). In addition, another peak was present 30° away from the normal direction (ND) towards the RD. This was in accordance with the {90°, 30°, 0} $_{\alpha'}$ component showing a similar intensity of ~3.0 times random for the corresponding $\phi_2 = 0°$ section (Fig. 7a). On the other hand, the sample having undergone 0.3 strain showed a higher intensity of ~7.1 MRD for {90°, 30°, 0}$_{\alpha'}$ and ~2.0 for {90°, 90°, 0}$_{\alpha'}$ components (Fig. 7b). With an increase in the strain to 1, the $(0001)_{\alpha'}$ texture showed a strong {90°, 90°, 0}$_{\alpha'}$ component with an intensity of ~15.1 MRD and a weaker {90°, 30°, 0}$_{\alpha'}$ component with an intensity of ~6.5 MRD (Fig. 7c).

3.2. Grain boundary character distribution

3.2.1. The intervariant boundary distribution

The misorientation angle distribution of the martensite formed through the different thermomechanical routes revealed four major peaks around the positions of ~10°, 55–65° and ~90° (Fig. 8a). These distributions were significantly different from what is expected from a random distribution in a polycrystal not formed by transformation. The misorientation axis corresponding to each misorientation angle peak was clustered around those expected from the Burgers OR [21]. It should be mentioned that no signs of misoreination angle/axis pairs corresponding to compressive and tensile twins were observed within the distribution. Although the misorientation angle and axis were similar for all conditions, the fraction of boundaries with misorientations near 63° peak increased with the strain.

Fig. 9 compares the theoretical fraction of the intervariant boundaries formed through the ideal Burgers OR with the experimental results. Here, the theoretical distribution of intervariant boundaries is referred to the calculated distribution considering no variant selection. Overall, the distribution of intervariants deviated from those calculated for all TMP conditions. The 63.26°/[$\bar{1}$0 5 5 $\bar{3}$] and the 60°/[1 1 $\bar{2}$ 0] intervariant boundaries had the highest and the second highest populations for all TMP conditions, respectively. On the other hand, the 10.53°/[0 0 0 1] intervariant had the lowest boundary fraction for all TMP conditions. The fraction for the 63.26°/[$\bar{1}$0 5 5 $\bar{3}$] intervariant boundary showed a gradual increase with an increase in strain (i.e., 0.38, 0.42 and 0.43 of the length fraction for the strain-free, 0.3 strain and 1 strain, respectively). On the other hand, the 60°/[1 1 $\bar{2}$ 0] intervariant boundary had a decreasing trend with strain, having 0.33, 0.30 and 0.29 of length fraction for the strain-free, 0.3 strain and 1 strain, respectively. The other intervariant boundary length fractions, naming 60.83°/

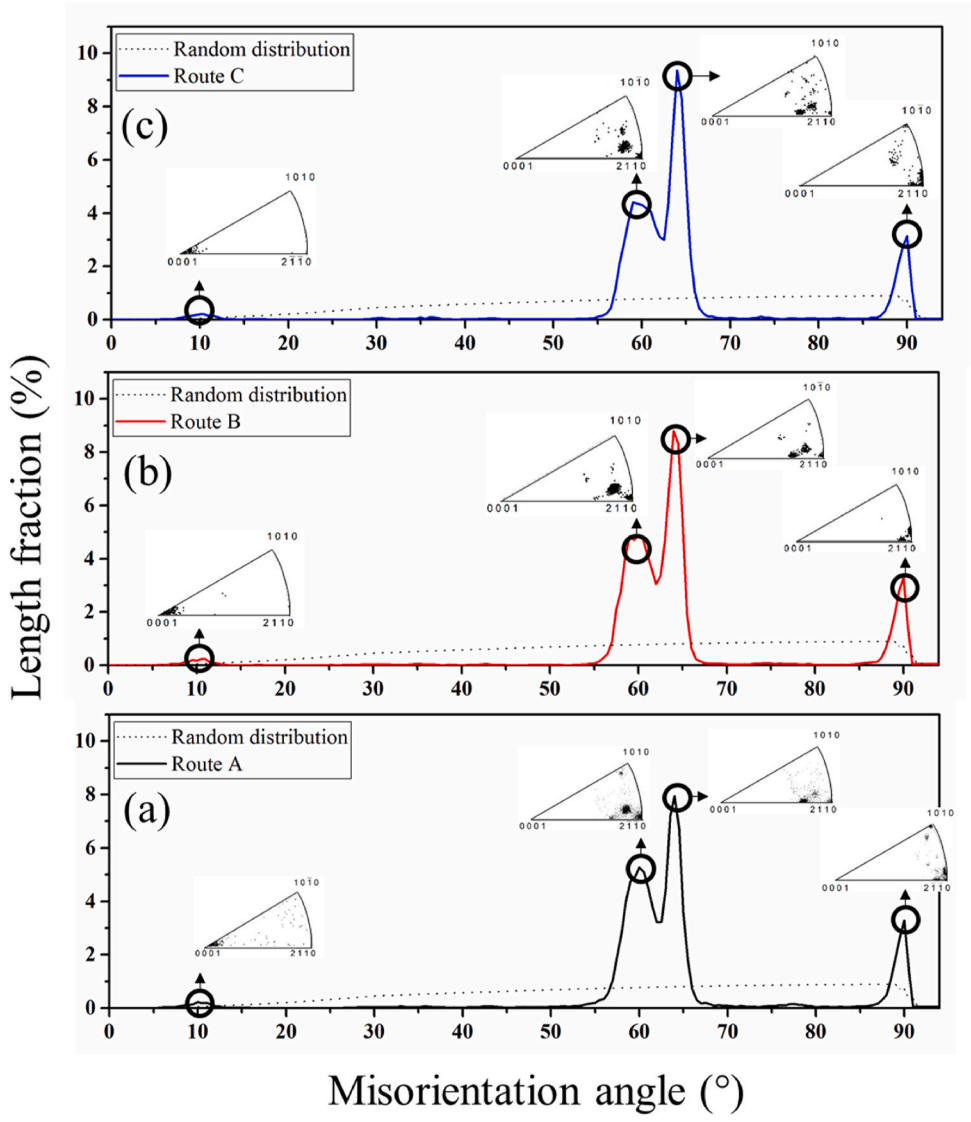

Fig. 8. The misorientation angle distribution and the misorientation axis distribution related to the misorientation angle peaks at 10°, 60°, 63° and 90° for Ti–6Al–4V martensite formed through different thermomechanical processing routes: (a) strain-free, (b) strain of 0.3 and (c) strain of 1. The dashed line is the representation of the random distribution of the misorientation angle for the hexagonal material.

$[\overline{1.377}\ \bar{1}\ 2.377\ 0.359]$ and $90°/[1\ \overline{2.38}\ 1.38\ 0]$, did not have a specific trend with strain.

3.2.2. The intervariant boundary plane distribution

The relative areas of all boundary planes, without considering the related misorientation of the boundaries, are depicted in a stereographic projection view within a hexagonal crystal reference frame (Fig. 10). The plot revealed an anisotropic distribution of martensite boundary planes formed through all TMP conditions, having their maximum intensities around the prismatic orientations along $\{1\ 0\ \bar{1}\ 1\}$ and $\{1\ 1\ \bar{2}\ 0\}$ boundary planes. Overall, the boundary plane distribution showed a slight decrease in the intensity from ~2 MRD in the strain-free condition to ~1.9 and ~1.8 MRD in the strains of 0.3 and 1, respectively. Similar to the boundary plane distribution for the CP-Ti alloy [21], the distribution minimum was located at the $(0\ 0\ 0\ 1)$ orientation for all processing routes (Fig. 10).

The boundary plane distribution was plotted on a stereographic projection for each intervariant boundary associated with the Burgers OR. The distributions were also compared with the corresponding characteristic grain boundary plane distribution provided by Glowinski's grain boundary toolbox software (Fig. 11) [45]. Overall, the grain boundary plane distribution of a given intervariant boundary was similar for all TMP conditions. However, the processing route significantly influenced the maxima. For all processing routes, the population of the $10.53°/[0\ 0\ 0\ 1]$ intervariant boundary was relatively low (i.e., ~2%), and no maxima higher than 0.5 MRD was observed in the distribution. Therefore, the $10.53°/[0\ 0\ 0\ 1]$ intervariant boundary was not further analysed in the current study. The distribution of intervariant boundary planes with a misorientation of $60°/[1\ 1\ \bar{2}\ 0]$ showed a single peak near the pyramidal $(\bar{1}\ 1\ 0\ 1)$ plane for all processing routes. However, the peak intensity for the strain-free condition was 370 MRD (Fig. 11a), while it progressively dropped at the 0.3 and 1 strain values, showing a maximum value of 349 MRD (Figs. 11b) and 294 MRD (Fig. 11c), respectively. The peak at the $(\bar{1}101)$ orientation had the ideal symmetric tilt boundary, also having 180°-twist and 180°-tilt character. The boundary plane distribution for the $60.83°/[\overline{1.377}\ \bar{1}\ 2.377\ 0.359]$ intervariant boundary had a maximum near the $(\bar{3}210)$ plane with an intensity of 24 MRD (Figs. 11d), 22 MRD (Fig. 11d–f) and 19 MRD (Fig. 11d–f) for the strain-free, strain of 0.3 and strain of 1, respectively. This boundary deviated by ~4° from the $(\bar{5}320)$ tilt boundary, which is also within the experimental resolution (Fig. 11d–f). For the

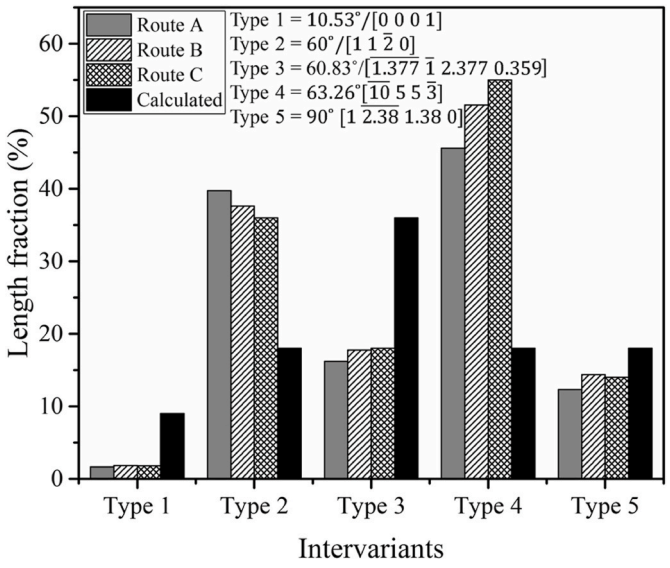

Fig. 9. The length fraction of the intervariant boundaries expected from the Burgers orientation relationship in martensite formed through different thermomechanical routes (i.e., strain free, strain 0.3 and strain 1). The solid black bar represents the theoretically calculated intervariant fractions, assuming the variant formation has a similar statistical probability during the β→α transformation.

63.26°/[$\overline{10}$ 5 5 $\bar{3}$] intervariant boundary, there was a peak close to the ($\bar{3}$ 2 1 0) plane showing an intensity of 577 MRD, 678 MRD and 576 MRD for the strain-free (Fig. 11g), strain of 0.3 (Fig. 11h) and strain of 1 (Fig. 11i), respectively. The orientation had a quasi-symmetric tilt or twist character (Fig. 11g–i). The intervariant plane distribution for the 90°/[1 $\overline{2.38}$ 1.38 0] had a diffuse maximum at the (17 $\overline{17}$ 0 18) plane (near (1 $\bar{1}$ 0 1) plane) with maximum intensities of 30 MRD, 38 MRD and 34 MRD for the strain-free, strain of 0.3 and strain of 1, respectively. This boundary plane orientation also had a twist and 180°-tilt character, spreading between the (1 $\bar{2}$ 1 3) and ($\bar{4}$ 3 $\bar{1}$ 0) planes (Fig. 11).

3.3. Grain boundary network connectivity

The number fraction of different classes of triple junctions for all five types of intervariant boundaries are displayed in Fig. 12 for the different TMP conditions. The thermomechanical processing had a minimal effect on the different triple junction classifications. Similar to the martensitic Ti–6Al–4V sample at the strain-free condition, the deformed samples had, around 10% of the triple junctions were made up entirely of either 60°/[11$\bar{2}$0] or 63.26°/[$\overline{10}$ 5 5 $\bar{3}$] intervariant boundaries (i.e., class 3 triple junction). On the other hand, most triple junctions were in the class 1 category, meaning that the triple junctions had only one intervariant boundary type.

Based on the results obtained from boundary plane distributions (Fig. 11), each intervariant boundary showed a single maximum (i.e., terminating by a specific plane orientation). In other words, the plane orientation of 60°/[1 1 $\bar{2}$ 0], 60.83°/[$\overline{1.377}$ $\bar{1}$ 2.377 0.359], 63.26°/[$\overline{10}$ 5 5 $\bar{3}$] and 90°/[1 $\overline{2.38}$ 1.38 0] are ($\bar{1}$ 1 0 1), ($\bar{5}$320), ($\bar{3}$ 2 1 0) and (1 $\bar{1}$ 0 1), respectively. This enables us to measure the average separation between intervarient boundary planes of the aforementioned planes using corresponding intervariant boundary lattice misorientation (Fig. 13). To measure the average separation between the intervariant boundary planes, the given misorientation angle/axis of an intervariant boundary was firstly filtered from the other intervariants and the mean linear intercept distance between boundaries was measured. Except for the 10.53°/[0 0 0 1] intervariant boundary, the application of strain gradually decreased the spacing among a specific intervariant boundary. In particular, the 63.26°/[$\overline{10}$ 5 5 $\bar{3}$] intervaraint boundary had the most dramatic decrease in the average separation with a ~50% reduction, meaning that thermomechanical processing resulted in a dense network of the highly populated 63.26°/[$\overline{10}$ 5 5 $\bar{3}$] intervariant boundary (i.e., finer microstructure). It should be considered that the decrease in separation of the bounray planes with the strain level requires a higher population density for the ($\bar{3}$ 2 1 0) boundary planes in the strain 1 compared to the strain 0.3 and strain-free samples. This is inconsstent with the boundary plane population depicted in (Fig. 11g–i). This inconsistency may require further 3D microstructure investigation to analyse the average boundary plane separation for both strain levels.

4. Discussion

The microstructural observations revealed that TMP significantly influences the overall texture (Fig. 7) but has a limited effect on the grain boundary network characteristics (i.e., population, plane orientation and connectivity, Fig. 12). The changes in the texture characteristics can be associated with alteration of the parent β texture due to the deformation and/or the preferred α′ variant nucleation on the active slip systems operating within the deformed parent β phase (i.e., variant selection). The latter is, to some extent, expected to change the grain boundary network, which is not the case in the current study. Therefore, the VPSC along with the forward-calculation approach was used to understand the extent of variant selection on the α′phase transformation texture for the different TMP conditions. This can be used to explain the grain boundary network characteristics for the different TMP conditions.

4.1. Texture evolution and variant selection during thermomechanical processing

The α′ texture characteristics in the strain-free condition are strongly

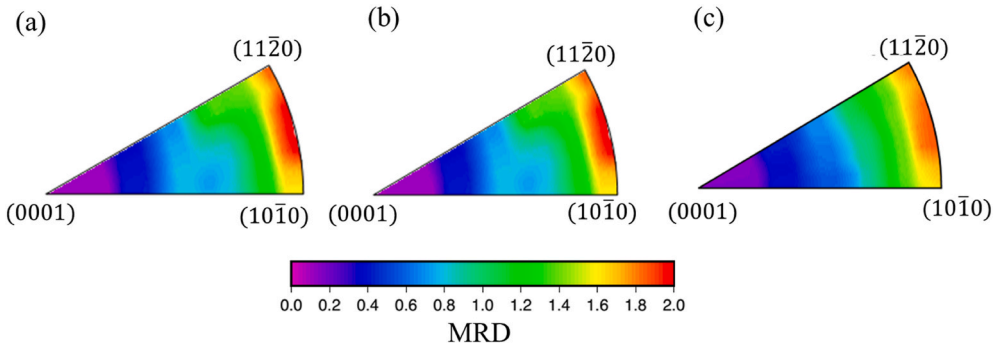

Fig. 10. The distribution of grain boundary planes considering all grain boundaries irrespective of their lattice misorientation for (a) strain-free, (b) strain of 0.3 and (c) strain of 1 conditions.

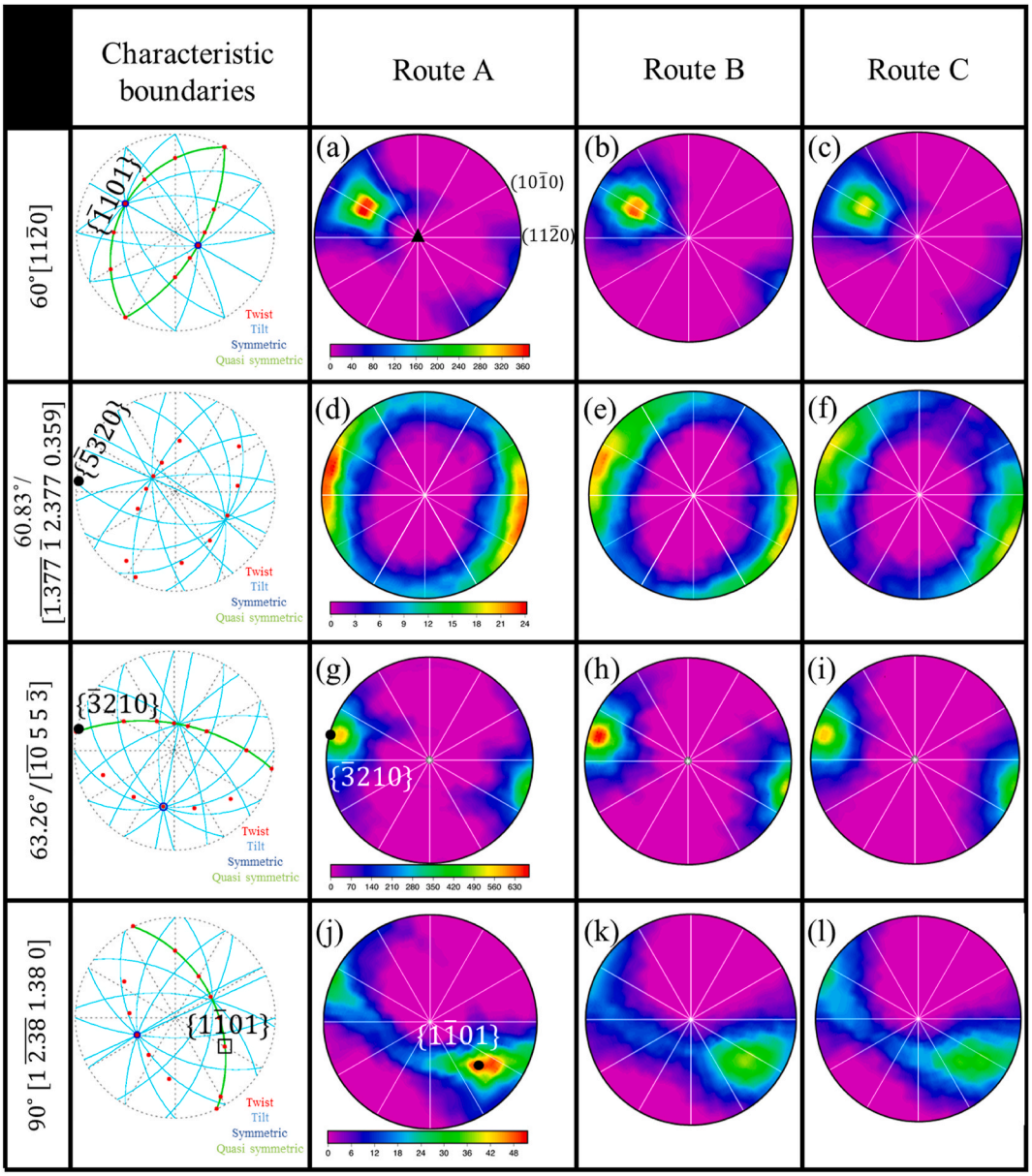

Fig. 11. The distribution of grain boundary planes at a fixed misorientation related to the intervariant boundaries of martensite formed through different thermomechanical routes, plotted in stereographic projection in the hexagonal crystal frame.

influenced by the growth of existing β phase in the as-received condition rather than the nucleation of new β grains from the as-received α phase structure [40,46]. Here, deformation of the alloy in the β phase provides a pronounced change in the qualitative characteristics of the overall α′ texture, largely displaying both {90°, 30°, 0°}$_{α'}$ and {90°, 90°, 0°}$_{α'}$ orientations in the (0001)$_{α'}$ pole figure (Fig. 7). The intensity of these orientations is significantly influenced by the processing route influence on the β phase. This means that the extent of slip system activity which alters the texture characteristic of the bcc structured parent phase plays an important role in defining the transformed α′ texture [47]. Also, the TMP treatment promotes defect structures within the parent β phase (sub-grains, deformation bands, etc.), which can be regarded as potential sites for α′ nucleation. Therefore, the analysis of variant selection in Ti–6Al–4V alloy requires an understanding of the role of texture and defects developed during the TMP treatment in the β phase region. In this regard, transformation texture modelling based on different active bcc slip systems was used to relate the ά variant nucleation to parent phase texture characteristics influenced by the slip system activity (i.e., variant selection mechanism).

The initial β microstructure consisted of 500 grains with equal size and was artificially constructed to represent the high temperature β overall texture (Fig. 14), similar to the experimental results reported earlier by our group (i.e., consisting of a main component of {112}$_β$ < 1$\bar{1}$0 >$_β$ at {0°, 33°, 45°}$_β$ orientations in (110)$_β$ pole figure with an overall intensity of ~4.1 MRD) [23]. It should be mentioned that the visualization of the VPSC simulations were conducted with the Atex software provided by Beausir [48]. The VPSC simulation was employed to simulate the overall texture of β at different deformed conditions, considering different combinations of preferred slip systems operating in high temperature deformation, namely {110}$_β$ < 111 >$_β$, {112}$_β$ < 111 >$_β$ and {123}$_β$ < 111 >$_β$ [49]. The simulated β texture was employed to compute the overall transformed α′ texture using the forward-calculation approach, assuming that each β grain transforms to 12 equally weighted distinct variants according to the Burgers OR (i.e., no variant selection).

The forward-calculation based on the Burgers OR shows that the

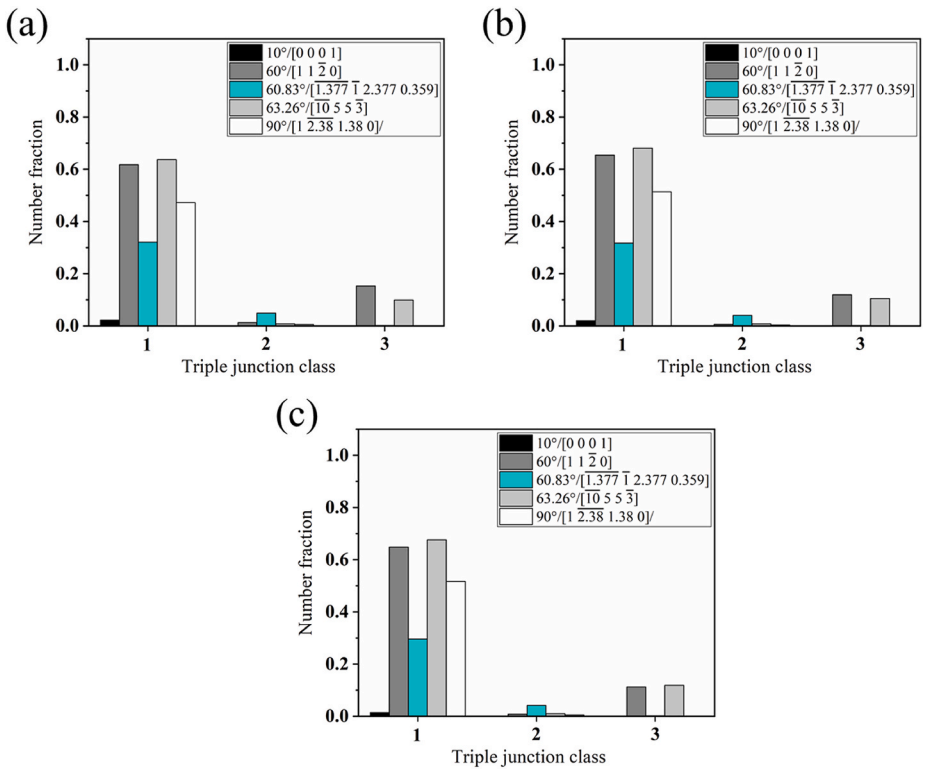

Fig. 12. (a–c) The classification of triple junctions as a function of intervariant boundary types and (a) strain-free, (b) strain of 0.3 and (c) strain of 1. Triple junction class 1 denotes the presence of only one intervariant boundary of interest and class 3 indicates that all the boundaries in the triple junction is the intervariant boundary of interest.

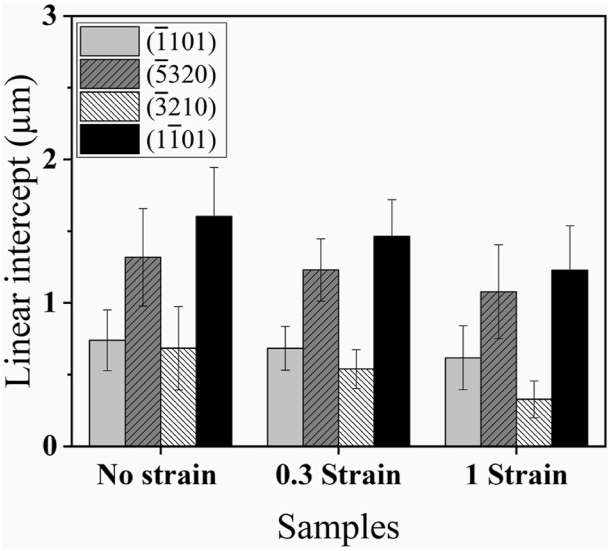

Fig. 13. The average separation between intervariant boundary planes. The ($\bar{1}$ 1 0 1), ($\bar{5}$320), ($\bar{3}$ 2 1 0) and (1 $\bar{1}$ 0 1) plane orientations correspond to 60°/[1 1 $\bar{2}$ 0], 60.83°/[$\overline{1.377}$ $\bar{1}$ 2.377 0.359], 63.26°/[$\overline{10}$ 5 5 $\bar{3}$] and 90°/[1 $\overline{2.38}$ 1.38 0], respectively.

characteristics of the overall α texture is closely related to the parent β texture for all operating slip system combinations, revealing {90°, 30°, 0°}$_{\alpha'}$ and {90°, 90°, 0°}$_{\alpha'}$ orientations in the (0001)$_{\alpha'}$ pole figure and the $\phi_2 = 0°$ sections of the ODF (Figs. 15–18). It should be emphasized that the magnitude of intensity change for each orientation was similar to the corresponding (110)$_{\beta}$ pole (Fig. 15). To better understand the occurrence of variant selection, the relative intensities of the {90°, 90°, 0°}$_{\alpha'}$ and {90°, 30°, 0°}$_{\alpha'}$ components for both experimental and simulated conditions were calculated and are given in Table 3. It should be noted that the transformation texture in the simulated condition was calculated considering no preference for variant selection. In the case of the strain-free condition, the relative intensity values were in close agreement (i.e., 0.70 and 0.67 in simulated and experimental conditions, respectively, Table 3), emphasizing that the simulation predicts very well the overall transformation texture using the β parent orientation. Obasi et al. [15], however, reported a preferred nucleation of α during the transformation of β upon slow cooling, as coarse beta grains were considered as the source of variant selection. However, the quantitative analysis of the current research is more in line with the previous findings [50], where minimal variant selection occurs with the coarse β grains under fast cooling processes (i.e., martensitic transformation).

According to the calculated values in Table 3, the experimental strain 0.3 condition has a relative intensity value of ~0.28, while the simulated texture showed higher values (i.e, 0.64–0.69) for all slip combination conditions. At the strain 1 condition, the relative intensity between the {90°, 90°, 0°}$_{\alpha'}$ and {90°, 30°, 0°}$_{\alpha'}$ components of the simulated texture reduces compared to the strain 0.3, but is still notably different from the experimental condition (Fig. 7 and Table 3). The simulated transformation textures reveal that the change in the activity of the operating slip systems has an insignificant role on the overall texture characteristics obtained for different TMP conditions of β phase (Figs. 15 and 16). This agrees with the findings of Semiatin et al. [50] who showed that the formed variants do not necessarily correlate with those of the highly activated β-phase slip systems. The comparison with experimental α′ textures reveals that the texture development during different TMP conditions is qualitatively similar to the simulation results (Fig. 7). However, the promotion of the {90°, 30°, 0°}$_{\alpha'}$ component at lower strain (i.e., strain 0.3) and the {90°, 90°, 0°}$_{\alpha'}$ at higher strain (i.e., strain 1) is more pronounced in the experimental observations. This discrepancy in the results can be linked to the formation of high dislocation

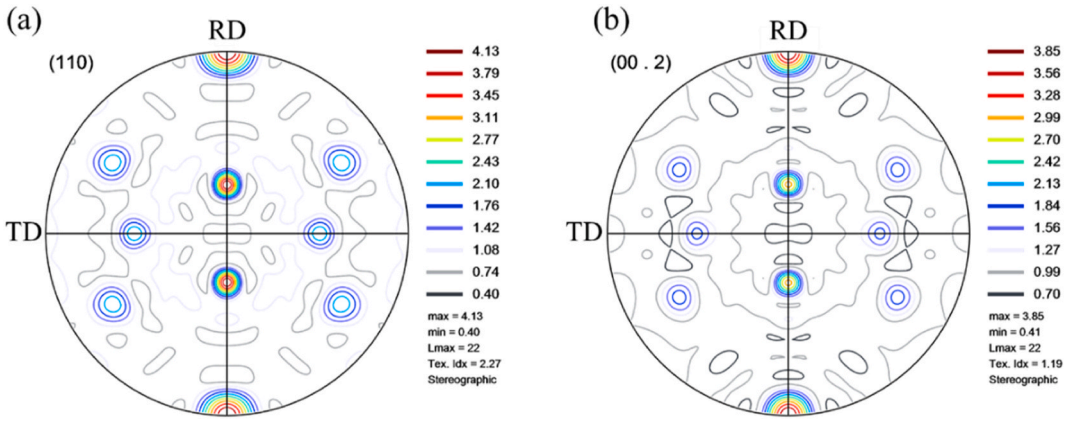

Fig. 14. (a) The (110) pole figure of artificially constructed high temperature β and (b) the forward calculated α texture after the β

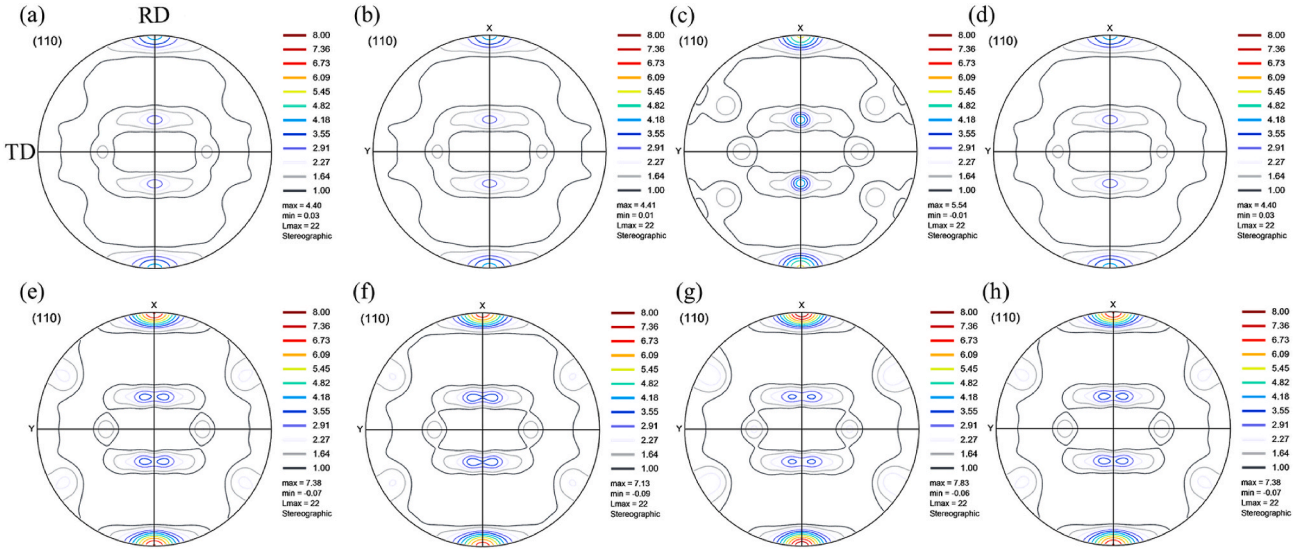

Fig. 15. The (110) pole figures of the simulated β texture at the (a–d) strain of 0.3 and (e–f) strain of 1for different slip system combinations: (a and e) {110}<111> + {112}<111>, (b and f) {110}<111> + {123}<111>, (c and g) {112}<111> + {123}<111>, (d and h) {110}<111> + {112}<111> + {123}<111>.

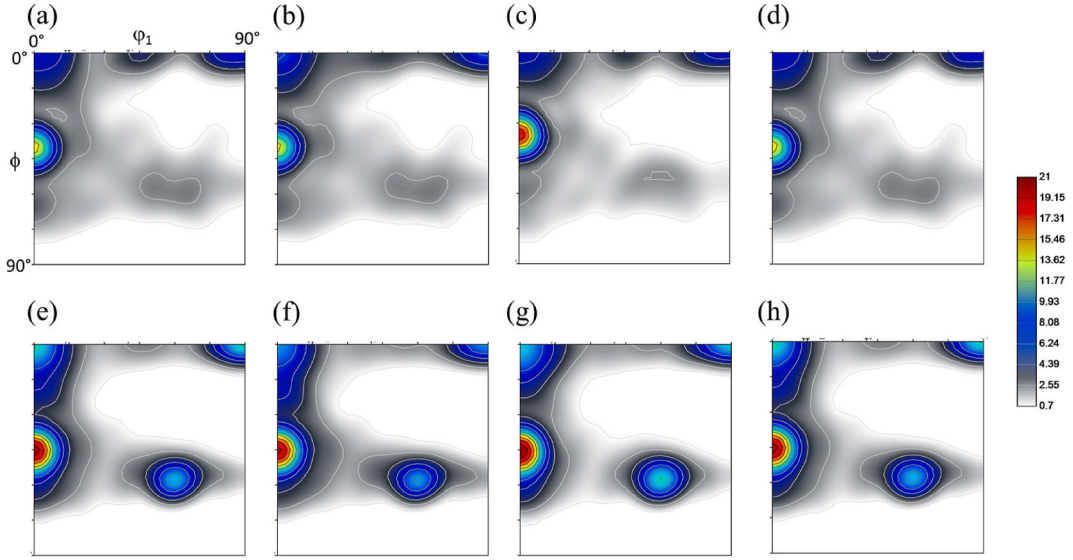

Fig. 16. The $\phi_2 = 45°$ Sections of the simulated β texture at the (a–d) strain of 0.3 and (e–f) strain of 1for different slip system combinations: (a and e) {110}<111> + {112}<111>, (b and f) {110}<111> + {123}<111>, (c and g) {112}<111> + {123}<111>, (d and h) {110}<111> + {112}<111> + {123}<111>.

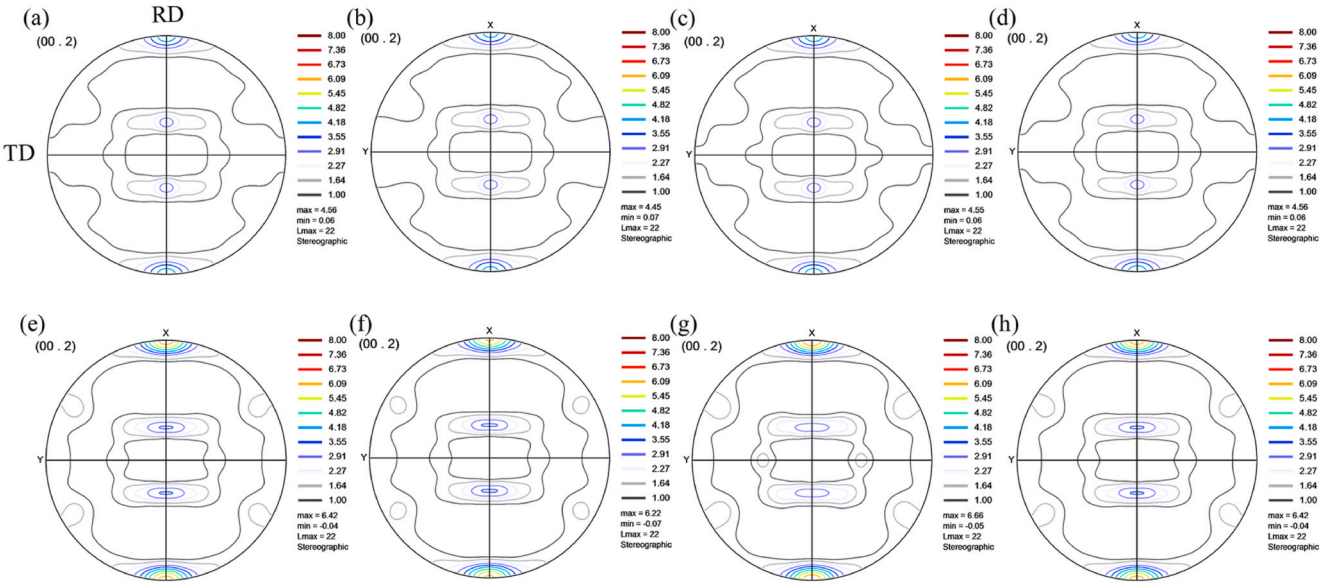

Fig. 17. The (0001) pole figures of the forward calculated ά texture at the (a–d) strain of 0.3 and (e–f) strain of 1 for different slip system combinations: (a and e) {110}<111> + {112}<111>, (b and f) {110}<111> + {123}<111>, (c and g) {112}<111> + {123}<111>, (d and h) {110}<111> + {112}<111> + {123}<111>.

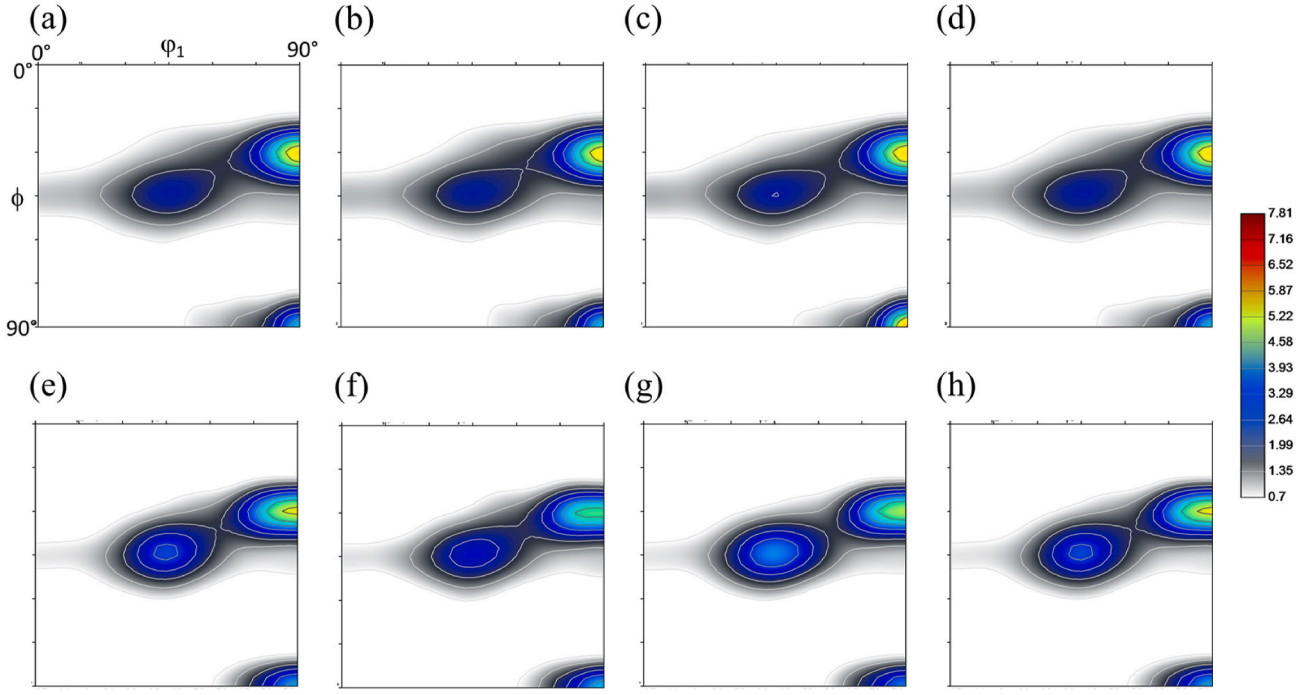

Fig. 18. The $\phi_2 = 0°$ Sections of the forward calculated α texture at the (a–d) strain of 0.3 and (e–f) strain of 1for different slip system combinations: (a and e) {110}<111> + {112}<111>, (b and f) {110}<111> + {123}<111>, (c and g) {112}<111> + {123}<111>, (d and h) {110}<111> + {112}<111> + {123}<111>.

density sites and lattice perturbations during TMP of the β phase, influencing the nucleation of the α′ variants [47,51–53]. In general, the α variants that have habit planes parallel or nearly parallel to the dislocation line are known to be favoured to nucleate and grow along the dislocation line, while variants with habit planes perpendicular to the dislocation line tend to grow into smaller laths [14,54]. The $\{110\}_\beta < 111 >_\beta$ slip system, for example, defines the β planes and directions of the Burgers OR, meaning that slip on a system like $(110)_\beta[\bar{1}1\bar{1}]_\beta$ can promote $(0002)_{\alpha'}[2\bar{1}10]_{\alpha'}$ variants. Besides, the Burgers OR is defined by the shear movement of atoms on the $\{112\}_\beta$ planes and $< 111 >_\beta$ directions [10], enforcing parallelism between the $(10\bar{1}0)_{\alpha'}$ and $(112)_\beta$ interfaces during the transformation. These planes correspond to the terraces of the broad face of the α variant, meaning that a particular $\{112\}_\beta < 111 >_\beta$ slip system can also promote specific α variant/s (i.e.,

variant selection). Therefore, the promotion of the $\{90°, 30°, 0°\}_{\alpha'}$ and $\{90°, 90°, 0°\}_{\alpha'}$ can be clearly attributed to the variant selection influenced by the defects formed along the active slip systems during the TMP treatment.

4.2. The role of TMP on the intervariant boundary network development in Ti–6Al–4V alloy

The overall texture is known to alter the grain boundary network in polycrystalline materials [55–57]. Despite a significant change in the transformed texture characteristics during thermomechanical processing in the current study (Fig. 7), the grain boundary network displays very limited changes with strain (Fig. 12). The enhancement of the $\{90°, 90°, 0\}_{\alpha'}$ and $\{90°, 30°, 0\}_{\alpha'}$ components is expected to increase the intersection of these variants during the transformation, leading to the promotion of the $60°/[11\bar{2}0]$ intervariant boundaries. However, this contradicts the current observation, as the length fraction of $60°/[11\bar{2}0]$ intervariant boundary gradually decreases with increasing strain (Fig. 9). By contrast, the $63.26°/[\bar{1}0\ 5\ 5\ \bar{3}]$ intervariant boundary population progressively increases with deformation, based on the disorientation distirbutions in Fig. 8.

In the strain-free condition, it is well known that a local variant selection takes place during the martensitic transformation in Ti–6Al–4V, promoting quadrilateral and/or V shape variant arrangement to minimise the transformation strain/energy [21]. This largely leads to the promotion of the $63.26°/[\bar{1}0\ 5\ 5\ \bar{3}]$, $60°/[11\bar{2}0]$ and $90°/[1\ \bar{2}.38\ 1.38\ 0]$ intervariant boundaries (Fig. 6d). The current result, therefore, suggests that the local variant arrangement (i.e., quadrilateral and/or V shape) is not specifically affected by the strain (Figs. 5 and 6), although the deformation of the β phase promotes similar quadrilateral variant clusters, consisting of variant/s having $\{90°, 90°, 0\}_{\alpha'}$ and/or $\{90°, 30°, 0\}_{\alpha'}$ orientations to minimise strain associated with both deformation and transformation. In other words, the shear occurring during the martenstic transformation of β-to-α′ for different deformation conditions still leads to local quadrilateral and/or V shape variant clusters, promoting similar triple junction arrangements (i.e., similar grain boundary network, Fig. 12).

In addition, the intervariant boundary plane distributions are qualitatively similar for all thermomechanical conditions, suggesting that the strain does not alter the grain boundary plane for a given lattice misorientation (Figs. 10 and 11). They are largely related to the crystallographic constraints associated with the Burgers OR rather than a low energy interface configuration, as demonstrated in our earlier works [20–22]. There is one exception related to $60°/[11\bar{2}0]$ terminated at $(\bar{1}101)$ having a low energy configuration. Interestingly, the intensity of the $(\bar{1}101)$ peak progressively decreases with strain (Fig. 11 a-c), which is closely related to its population trend for the different TMP conditions (Fig. 9). On the other hand, the spacing between the intervariant planes (Fig. 13), regardless of the character, is being reduced by higher TMP strains, indicating the possible formation of a dense network of boundary planes during thermomechanical processing of the Ti–6Al–4V alloy.

The findings presented in this study reveal that the TMP processing conditions can be influential in changing the overall texture characteristics of the martensitic Ti through promoting variant selection on specific slip systems. However, the grain boundary network characteristics are purely controlled by the crystallographic strains associated with the phase transformation. This means that the main factor in defining the grain boundary network in martensitic Ti is the promotion of local variant selection by the transformation strain. This important finding provides a path to control the grain boundary network during the TMP treatment of Ti alloys, as it controls the material property performance.

5. Conclusion

The characteristics of the martensite intervariant boundary network produced by the thermomechanical processing of a Ti–6Al–4V alloy were investigated by conventional EBSD mapping along with five-parameter analysis of the boundary data. Moreover, the extent of variant selection occurring during the thermomechanical processing of Ti–6Al–4V and the subsequent $\beta \rightarrow \alpha'$ transformation was examined using VPSC simulation and forward calculation of the transformation texture. The following are the most important findings:

1) The results from the simulation, when compared to the observations, suggest that the α' transformed texture was influenced by both the deformed β parent texture and variant selection.
2) Thermomechanical processing changed the grain boundary misorientation angle distribution in only a limited way. The highest fraction of the boundaries was associated with the $63.26°/[\bar{1}0553]$ misorientation, which increased with the strain level. This was in accordance with the quadrilateral and/or V like variant combinations observed in the martensitic microstructure.
3) The boundary plane distribution associated with different thermomechanical processing regimes showed similar boundary plane orientations for all misorientations. The employment of higher strain levels resulted into a decreased fraction of the lower energy $(\bar{1}\ 1\ 0\ 1)$ interfaces associated with the symmetric tilt $60°/[1\ 1\ \bar{2}\ 0]$ intervariant boundaries.
4) The grain boundary network (i.e., triple junction arrangement) largely remained similar for all thermomechanical conditions, as the quadrilateral and/or V shape variant arrangement was a dominant feature for all microstructures produced through the different TMP routes. In other words, the elastic interactions of the variants during the martensitic transformation was the dominant parameter affecting the grain boundary network, despite the presence of variant selection due to the strain.

Data availability statement

The raw/processed data required to reproduce these findings cannot be shared at this time as the data also forms part of an ongoing study.

CRediT authorship contribution statement

Ehsan Farabi: Formal analysis, Investigation, Data curation, Writing – original draft, Writing – review & editing. **Vahid Tari:** Data curation, Validation. **Peter D. Hodgson:** Conceptualization, Data curation, Writing – review & editing, Supervision. **Gregory S. Rohrer:** Conceptualization, Data curation, Writing – review & editing. **Anthony D. Rollett:** Conceptualization, Writing – review & editing. **Hossein Beladi:** Methodology, Conceptualization, Formal analysis, Investigation, Data curation, Writing – original draft, Writing – review & editing, Supervision.

Declaration of competing interest

The authors declare that they have no known competing financial interests or personal relationships that could have appeared to influence the work reported in this paper.

Acknowledgements

Deakin University's Advanced Characterization Facility is acknowledged for use of the EBSD instruments and assistance from Dr. Mark Nave. The authors also thank Mahmoud Reza Ghandehari Ferdowsi for his assistance on TEM analysis.

References

[1] D. Banerjee, J.C. Williams, Perspectives on titanium science and technology, Acta Mater. 61 (2013) 844–879, https://doi.org/10.1016/j.actamat.2012.10.043.
[2] G. Lütjering, J.C. Williams, Titanium, Springer Science & Business Media, 2007.
[3] M.J. Donachie, Titanium: a Technical Guide, ASM international, 2000.
[4] S.L. Semiatin, V. Seetharaman, I. Weiss, The thermomechanical processing of alpha/beta titanium alloys, J. Miner. Met. Mater. Soc. 49 (1997) 33–39, https://doi.org/10.1007/BF02914711.
[5] E. Ghasemi, A. Zarei-Hanzaki, E. Farabi, K. Tesař, A. Jäger, M. Rezaee, Flow softening and dynamic recrystallization behavior of BT9 titanium alloy: a study using process map development, J. Alloys Compd. 695 (2017), https://doi.org/10.1016/j.jallcom.2016.10.322.
[6] I. Lonardelli, N. Gey, H.R. Wenk, M. Humbert, S.C. Vogel, L. Lutterotti, In situ observation of texture evolution during α→β and β→α phase transformations in titanium alloys investigated by neutron diffraction, Acta Mater. 55 (2007) 5718–5727, https://doi.org/10.1016/j.actamat.2007.06.017.
[7] M.R. Daymond, R.A. Holt, S. Cai, P. Mosbrucker, S.C. Vogel, Texture inheritance and variant selection through an hcp-bcc-hcp phase transformation, Acta Mater. 58 (2010) 4053–4066, https://doi.org/10.1016/j.actamat.2010.03.012.
[8] N. Gey, M. Humbert, H. Moustahfid, Study of the α→β phase transformation of a Ti-6Al-4V sheet by means of texture change, Scripta Mater. 42 (2000) 525–530, https://doi.org/10.1016/S1359-6462(99)00396-6.
[9] Q. Chao, P.D. Hodgson, H. Beladi, Microstructure and texture evolution during symmetric and asymmetric rolling of a martensitic Ti-6Al-4V alloy, Metall. Mater. Trans. 47 (2016) 531–545, https://doi.org/10.1007/s11661-015-3211-y.
[10] W.G.G. Burgers, On the process of transition of the cubic-body-centered modification into the hexagonal-close-packed modification of zirconium, Physica 1 (1934) 561–586, https://doi.org/10.1016/S0031-8914(34)80244-3.
[11] X. Zhong, D.J. Rowenhorst, H. Beladi, G.S. Rohrer, The five-parameter grain boundary curvature distribution in an austenitic and ferritic steel, Acta Mater. 123 (2017) 136–145, https://doi.org/10.1016/j.actamat.2016.10.030.
[12] D. Qiu, P. Zhao, R. Shi, Y. Wang, W. Lu, Effect of autocatalysis on variant selection of α precipitates during phase transformation in Ti-6Al-4V alloy, Comput. Mater. Sci. 124 (2016) 282–289, https://doi.org/10.1016/j.commatsci.2016.07.032.
[13] R. Shi, Y. Zheng, D. Wang, H. Fraser, Y. Wang, I. Nucleation, N. Band, M. Field, A. I, Energy, heterogenous nucleation during in titanium alloys transformation, Proc. 13th World Conf. Titan. 1 (2016) 1931–1936, https://doi.org/10.1002/9781119296126.ch323.
[14] D. Qiu, R. Shi, D. Zhang, W. Lu, Y. Wang, Variant selection by dislocations during α precipitation in α/β titanium alloys, Acta Mater. 88 (2015) 218–231, https://doi.org/10.1016/j.actamat.2014.12.044.
[15] G.C. Obasi, S. Birosca, J. Quinta Da Fonseca, M. Preuss, Effect of β grain growth on variant selection and texture memory effect during α→β→α phase transformation in Ti-6 Al-4 v, Acta Mater. 60 (2012) 1048–1058, https://doi.org/10.1016/j.actamat.2011.10.038.
[16] S.C. Wang, M. Aindow, M.J. Starink, Effect of self-accommodation on α/α boundary populations in pure titanium, Acta Mater. 51 (2003) 2485–2503, https://doi.org/10.1016/S1359-6454(03)00035-1.
[17] N. Stanford, P.S. Bate, Crystallographic variant selection in Ti-6Al-4V, Acta Mater. 52 (2004) 5215–5224, https://doi.org/10.1016/j.actamat.2004.07.034.
[18] D. Bhattacharyya, G.B. Viswanathan, H.L. Fraser, Crystallographic and morphological relationships between β phase and the Widmanstatten and allotriomorphic α phase at special β grain boundaries in an α/β titanium alloy, Acta Mater. 55 (2007) 6765–6778, https://doi.org/10.1016/j.actamat.2007.08.029.
[19] M. Shibata, K. Ono, On the minimization of strain energy in the martensitic transformation of titanium, Acta Metall. 25 (1977) 35–42, https://doi.org/10.1016/0001-6160(77)90243-7.
[20] E. Farabi, V. Tari, P.D. Hodgson, G.S. Rohrer, H. Beladi, The role of phase transformation mechanism on the grain boundary network in a commercially pure titanium, Mater. Char. 169 (2020) 110640, https://doi.org/10.1016/j.matchar.2020.110640.
[21] E. Farabi, P.D. Hodgson, G.S. Rohrer, H. Beladi, Five-parameter intervariant boundary characterization of martensite in commercially pure titanium, Acta Mater. 154 (2018) 147–160, https://doi.org/10.1016/j.actamat.2018.05.023.
[22] E. Farabi, V. Tari, P.D. Hodgson, G.S. Rohrer, H. Beladi, On the grain boundary network characteristics in a martensitic Ti-6Al-4V alloy, J. Mater. Sci. 55 (2020) 15299–15321, https://doi.org/10.1007/s10853-020-05075-7.
[23] H. Beladi, Q. Chao, G.S. Rohrer, Variant selection and intervariant crystallographic planes distribution in martensite in a Ti-6Al-4V alloy, Acta Mater. 80 (2014) 478–489, https://doi.org/10.1016/j.actamat.2014.06.064.
[24] P.L. Stephenson, N. Haghdadi, R. DeMott, X.Z. Liao, S.P. Ringer, S. Primig, Effect of scanning strategy on variant selection in additively manufactured Ti-6Al-4V, Addit. Manuf. 36 (2020) 101581, https://doi.org/10.1016/j.addma.2020.101581.
[25] N. Haghdadi, R. DeMott, P.L. Stephenson, X.Z. Liao, S.P. Ringer, S. Primig, Five-parameter characterization of intervariant boundaries in additively manufactured Ti-6Al-4V, Mater. Des. 196 (2020) 109177, https://doi.org/10.1016/j.matdes.2020.109177.
[26] T. Furuhara, H. Nakamori, T. Maki, Crystallography of α phase precipitated on dislocations and deformation twin boundaries in a β titanium alloy, Mater. Trans. 33 (1992) 585–595, https://doi.org/10.2320/matertrans1989.33.585.
[27] R. Shi, V. Dixit, H.L. Fraser, Y. Wang, Variant selection of grain boundary α by special prior β grain boundaries in titanium alloys, Acta Mater. 75 (2014) 156–166, https://doi.org/10.1016/j.actamat.2014.05.003.
[28] M. Salib, J. Teixeira, L. Germain, E. Lamielle, N. Gey, E. Aeby-Gautier, Influence of transformation temperature on microtexture formation associated with α precipitation at β grain boundaries in a β metastable titanium alloy, Acta Mater. 61 (2013) 3758–3768, https://doi.org/10.1016/j.actamat.2013.03.007.
[29] T. Furuhara, T. Maki, Variant selection in heterogeneous nucleation on defects in diffusional phase transformation and precipitation, Mater. Sci. Eng. 312 (2001) 145–154, https://doi.org/10.1016/S0921-5093(00)01904-3.
[30] N. Gey, M. Humbert, Characterization of the variant selection occurring during the α to β phase transformations of a cold rolled titanium sheet, Acta Mater. 50 (2002) 277–287, https://doi.org/10.1016/S1359-6454(01)00351-2.
[31] N. Gey, M. Humbert, M.J. Philippe, Y. Combres, Modeling the transformation texture of Ti-64 sheets after rolling in the β-field, Mater. Sci. Eng. 230 (1997) 68–74, https://doi.org/10.1016/S0921-5093(97)80111-6.
[32] S.L. Semiatin, K.T. Kinsel, A.L. Pilchak, G.A. Sargent, Effect of process variables on transformation-texture development in Ti-6Al-4V sheet following beta heat treatment, Metall. Mater. Trans. A Phys. Metall. Mater. Sci. 44 (2013) 3852–3865, https://doi.org/10.1007/s11661-013-1735-6.
[33] M. Kato, S. Onaka, T. Fujii, Energy consideration for variant selection in precipitation on dislocations, Sci. Technol. Adv. Mater. 2 (2001) 375–380.
[34] M.P. Butron-Guillen, C.S. Da Costa Viana, J.J. Jonas, A variant selection model for predicting the transformation texture of deformed austenite, Metall. Mater. Trans. 28A (1997) 1755–1768, https://doi.org/10.1007/s11661-997-0107-5.
[35] V. Tari, A.D. Rollett, H. Beladi, Back calculation of parent austenite orientation using a clustering approach, J. Appl. Crystallogr. 46 (2013) 210–215, https://doi.org/10.1107/s002188981204914x.
[36] R.A. Lebensohn, C.N. Tomé, A self-consistent anisotropic approach for the simulation of plastic deformation and texture development of polycrystals: application to zirconium alloys, Acta Metall. Mater. 41 (1993) 2611–2624, https://doi.org/10.1016/0956-7151(93)90130-K.
[37] D.M. Saylor, B.S. El-Dasher, B.L. Adams, G.S. Rohrer, Measuring the five-parameter grain-boundary distribution from observations of planar sections, Metall. Mater. Trans. 35 (2004) 1981–1989, https://doi.org/10.1007/s11661-004-0147-z.
[38] C.N. Tomé, R.A. Lebensohn, Visco-plastic self-consistent (vpsc), Los Alamos Natl. Lab. Univ. Nac. Rosario. 6 (2007).
[39] S. Takajo, S.C. Vogel, C.N. Tome, Viscoplastic self-consistent polycrystal modeling of texture evolution of ultra-low carbon steel during cold rolling, Model. Simulat. Mater. Sci. Eng. 27 (2019) 45003.
[40] G.C. Obasi, R.J. Moat, D.G. Leo Prakash, W. Kockelmann, J. Quinta Da Fonseca, M. Preuss, In situ neutron diffraction study of texture evolution and variant selection during the α→β→α phase transformation in Ti-6Al-4V, Acta Mater. 60 (2012) 7169–7182, https://doi.org/10.1016/j.actamat.2012.09.026.
[41] M. Peters, A. Gysler, G. Lutjering, Influence of texture on fatigue properties of Ti-6Al-4V, Metall. Mater. Trans. 15 (1984) 1597–1605, https://doi.org/10.1007/BF02657799.
[42] A. Zarkades, F.R. Larson, Texture of Ti-6Al-4V as Affected by Rolling Temperature, 1975, p. 8.
[43] H.J.G. Gundersen, T.B. Jensen, R. Østerby, Distribution of membrane thickness determined by lineal analysis, J. Microsc. 113 (1978) 27–43, https://doi.org/10.1111/j.1365-2818.1978.tb00091.x.
[44] J. Tiley, T. Searles, E. Lee, S. Kar, R. Banerjee, J.C. Russ, H.L. Fraser, Quantification of microstructural features in α/β titanium alloys, Mater. Sci. Eng. 372 (2004) 191–198, https://doi.org/10.1016/j.msea.2003.12.008.
[45] K. Glowinski, A. Morawiec, A toolbox for geometric grain boundary characterization, in: Proc. 1st Int. Conf. 3D Mater. Sci, Springer, Cham, 2012, pp. 119–124.
[46] G.C. Obasi, J.Q. da Fonseca, D. Rugg, M. Preuss, The effect of β grain coarsening on variant selection and texture evolution in a near-β Ti alloy, Mater. Sci. Eng. 576 (2013) 272–279, https://doi.org/10.1016/j.msea.2013.04.018.
[47] N. Gey, M. Humbert, M.J. Philippe, Y. Combres, Modeling the transformation texture of Ti-64 sheets after rolling in the β-field, Mater. Sci. Eng. 230 (1997) 68–74, https://doi.org/10.1016/S0921-5093(97)80111-6.
[48] B. Beausir, J.J. Fundenberger, Analysis Tools for Electron and X-Ray Diffraction, ATEX-Software, Univ. Lorraine-Metz, 2017.

[49] E.A. Calnan, C.J.B. Clews, LXV. The development of deformation textures in metals.— *Part II* . Body-centred cubic metals, London, Edinburgh, Dublin Philos. Mag. J. Sci. 42 (1951) 616–635, https://doi.org/10.1080/14786445108561277.
[50] S.L. Semiatin, K.T. Kinsel, A.L. Pilchak, G.A. Sargent, Effect of process variables on transformation-texture development in Ti-6Al-4V sheet following beta heat treatment, Metall. Mater. Trans. A Phys. Metall. Mater. Sci. 44 (2013) 3852–3865, https://doi.org/10.1007/s11661-013-1735-6.
[51] N. Gey, M. Humbert, M.J. Philippe, Y. Combres, Investigation of the α- and β-texture evolution of hot rolled Ti-64 products, Mater. Sci. Eng. 219 (1996) 80–88, https://doi.org/10.1016/S0921-5093(96)10388-9.
[52] I. Weiss, S.L. Semiatin, Thermomechanical processing of beta titanium alloys—an overview, Mater. Sci. Eng. 243 (1998) 46–65, https://doi.org/10.1016/S0921-5093(97)00783-1.
[53] N. Gey, M. Humbert, M.J. Philippe, Y. Combres, Modeling the transformation texture of Ti-64 sheets after rolling in the β-field, Mater. Sci. Eng. 230 (1997) 68–74.
[54] Z.Q. Feng, Y.Q. Yang, B. Huang, X. Luo, M.H. Li, M. Han, M.S. Fu, Variant selection and the strengthening effect of S precipitates at dislocations in Al-Cu-Mg alloy, Acta Mater. 59 (2011) 2412–2422, https://doi.org/10.1016/j.actamat.2010.12.041.
[55] H. Beladi, G.S. Rohrer, The role of thermomechanical routes on the distribution of grain boundary and interface plane orientations in transformed microstructures, Metall. Mater. Trans. 48 (2017) 2781–2790, https://doi.org/10.1007/s11661-016-3630-4.
[56] N. Haghdadi, P. Cizek, P.D. Hodgson, V. Tari, G.S. Rohrer, H. Beladi, Effect of ferrite-to-austenite phase transformation path on the interface crystallographic character distributions in a duplex stainless steel, Acta Mater. 145 (2018) 196–209, https://doi.org/10.1016/j.actamat.2017.11.057.
[57] N. Haghdadi, P. Cizek, P.D. Hodgson, V. Tari, G.S. Rohrer, H. Beladi, Five-parameter crystallographic characteristics of the interfaces formed during ferrite to austenite transformation in a duplex stainless steel, Philos. Mag. A 98 (2018) 1284–1306, https://doi.org/10.1080/14786435.2018.1434321.